ChemComm

FEATURE ARTICLE

Check for updates

Revealing the microstructure and mechanism of layered oxide cathodes for sodium-ion batteries by advanced TEM techniques

Sheng Xu,[a] Lihua Zhao,*[b] Shukui Li[c] and Shaohua Guo [ID] *[acd]

Sodium-ion batteries (SIBs) stand as promising alternatives to current lithium-ion batteries in various energy storage fields. Despite their potential, challenges arise due to the intricate nature of large-size Na$^+$ charge carriers, impacting the cycling stability and rate performance, which currently fall short of commercialization requirements. Therefore, it is crucial to gain a deeper understanding of the structural changes and chemical evolution of battery components. The advancement of transmission electron microscopy (TEM) technology enables multi-dimensional characterization and analysis of SIB cathode materials. This review offers an in-depth overview and comparison of the utilization of advanced TEM techniques for studying layered oxide cathode materials. It covers various aspects, including the common analysis of atomic structures, structural phase transitions, elemental valence tracing, and anion redox, and provides insights from current *in situ* TEM experiments. The presented review aims to provide valuable insights to inform the rational design of high-performance SIB cathodes.

1. Introduction

Growing concerns about the environment and the high energy needs of modern society are driving the development of alternative renewable energy sources, with rechargeable batteries as representatives. Sodium-ion batteries (SIBs) are considered as alternatives to the current lithium-ion batteries (LIBs) due to their abundant source, low cost, and safety properties.[1–3] To date, various types of electrodes for SIBs have been developed using carbon-based materials, intermetallic alloys, organic compounds, and transition metal oxides or sulfides.[4] Compared to anode materials, which already exhibit high specific capacities (≥ 300 mA h g^{-1}),[5,6] cathode materials typically provide 100–200 mA h g^{-1} specific capacities, significantly limiting the whole system energy density.[7] The key factors of SIBs are highly dependent on the cathode materials, including working voltage, energy density, and lifetime. The cathodes mainly consist of layered transition metal (TM) oxides, Prussian blue analogues, and polyanionic compounds.[8] Among these candidates, layered TM oxides show great prospects as commercial cathode materials for SIBs due to their high ionic conductivity, simple synthesis, and long working life. However, resulting from the large radius of Na$^+$ ions and low kinetics, the layered oxides suffer from several structural degradations, such as Jahn–Teller distortion, phase transformation, and surface decomposition.[9,10] Such fundamental issues should be addressed before full commercialization of SIBs.

The very first step is to figure out the structures of the observed layered oxides. Multi-dimensional imaging and spectroscopy characterization have been employed to study the structural evolution and reaction kinetics of cathode materials at various length scales. Current illustrative techniques include but are not limited to, magnetic resonance imaging (MRI), neutron diffraction, Raman spectroscopy, X-ray diffraction (XRD), X-ray absorption spectroscopy (XAS), scanning electron microscopy (SEM) and focused ion beam (FIB).[11] One should notice that these techniques typically provide structural and elemental information at a micrometer or larger scale, leading to the ignorance of fine structure information. Another issue is that these test results are derived from different samples, which may cause mismatched information. As a high-resolution imaging technique, transmission electron microscopy (TEM) overcomes these limitations to provide atomic structural features, for example, bulk phase, surface evolution, lattice distortions, boundaries, and elemental changes. Modern TEM instruments can provide

^{a} *College of Engineering and Applied Sciences, Jiangsu Key Laboratory of Artificial Functional Materials, National Laboratory of Solid State Microstructures, Collaborative Innovation Centre of Advanced Microstructures, Frontiers Science Center for Critical Earth Material Cycling, Nanjing University, Nanjing 210093, P. R. China. E-mail: shguo@nju.edu.cn*

^{b} *College of Art&Design, Nanjing Tech University, Nanjing, Jiangsu 211816, P. R. China. E-mail: reika2008@hotmail.com*

^{c} *Department of Materials Science, Shenzhen MSU-BIT University, Shenzhen 517182, P. R. China*

^{d} *Lab of Power and Energy Storage Batteries, Shenzhen Research Institute of Nanjing University, Shenzhen 518057, P. R. China*

sub-angstrom resolution, which enables atomic-precision imaging of both bulk and surface structures. Advanced TEM techniques combine real-space imaging with spectroscopy analysis, offering atomic-level insights into the physical structure and chemical properties of a specimen. By using the integration of *in situ* and *operando* devices, one can monitor the structural evolutions and property changes under working conditions.

TEM has become indispensable in nanomaterials research, and one can find more introductions concerning its history, techniques, and application in previous reviews.[12–14] This review will focus on the applications of TEM in layered oxides used as SIB cathodes, involving structural determination and chemical properties at the nanoscale. Such observations highly depend on the characterization at high-spatial resolution provided by TEM. Firstly, various TEM techniques for layered oxide characterization are introduced, emphasizing their capabilities and applications with illustrative examples. It then examines TEM applications in analysing intrinsic structures, observing evolution during charging states, and investigating failure mechanisms. Finally, our outlook and perspectives are offered on current challenges and the future role of TEM in uncovering design strategies for layered oxides.

2. TEM techniques

The major imaging modes of conventional TEM can be classified into two categories: TEM and scanning TEM (STEM). In the TEM mode, a parallel electron beam illuminates the specimen and the transmitted electrons fall onto the camera to form a bright-field image. At low magnifications, the TEM image is used to distinguish the crystalline and amorphous phases, such as the cathode–electrolyte interface (CEI), surface coating, or surface phase change, and can provide phase-contrast images to determine the crystal structures. The selected-area electron diffraction (SAED) patterns can be collected at the back focal plane, which show the periodical information of the selected particles. The fundamentals of SAED are similar to those of XRD, in which the phases or the structures can be defined. For layered oxides, the phase transformation sometimes can be hardly detected by XRD or requires a high signal/noise ratio. By using the 3D tomography technique, the single particle can be visualized in a 3D model with each facet determined, rather than a single TEM projection image.

In the STEM mode, as shown in Fig. 1, the convergent electron beam interacts with the specimen, generating secondary particles to form images and for spectroscopy analysis. After interaction with the specimen, part of the primary electrons is scattered and collected at different detectors based on the scattering angles, bright-field (BF), annular bright field (ABF), annular dark field (ADF), and high-angle annular dark field (HAADF). For layered oxides, STEM-HAADF is most used to reveal the TM ions and their ordering, in which the image contrast is proportional to $Z^{1.7}$ (Z represents the atomic number).[15] STEM-ABF imaging has also been well used in
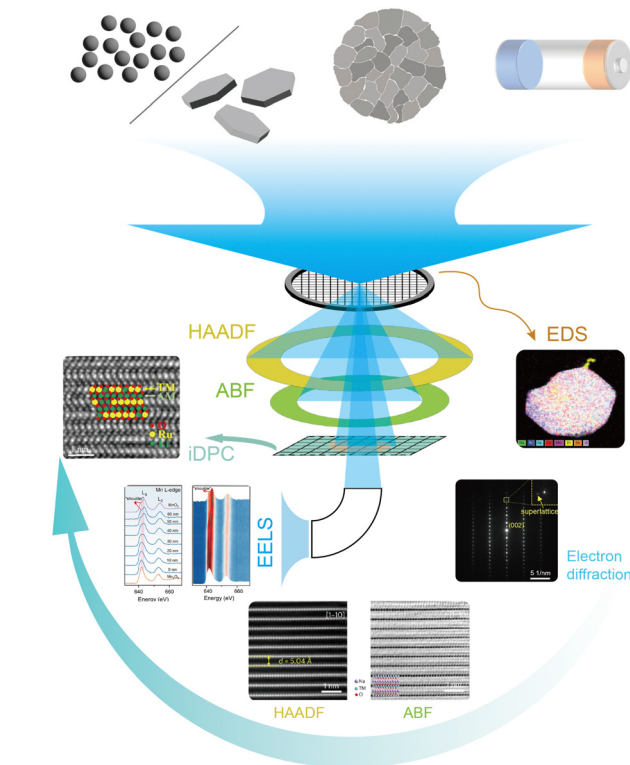

**Fig. 1** Summary of TEM applications for the study of layered oxides.

locating the light elements, such as oxygen and lithium in the electrode materials.[16–18]

Coupling with spectroscopic functionalities, TEM offers the elemental composition along with complex structures of layered oxides at atomic scale resolution. Energy dispersive X-ray spectroscopy (EDS) and electron energy loss spectroscopy (EELS) are the most commonly used techniques with TEM. In the EDS technique, high-energy electrons interact with sample atoms, displacing low-orbit electrons. Subsequently, higher-orbit electrons fill the vacancies, emitting X-rays in the process. Each element produces a distinct identification peak, and the elements can be determined by fitting the peak values in the spectra to a database. A common use is to determine the distribution of TM, Na, and O elements since EDS is more sensitive to heavy atoms ($Z > 5$). On the other hand, the EELS spectrum corresponds to the recording of the primary process of the electron excitation process with target atoms. The incident electron will transfer an appreciable amount of energy to the orbiting electron, thus exciting them to higher energy levels during the inelastic interaction process. The main functions of EELS include the analysis of chemical bonding, valence states of TM ions, and electronic structures.

3. Structural investigation in Na$_x$TMO$_2$

3.1 Typical P2 and O3 phases

The layered TM oxides used in SIBs are normally characterized by the general formula Na$_x$TMO$_2$ ($0 < x < 1$), and are constructed through the repetitive stacking of edge-sharing
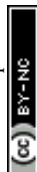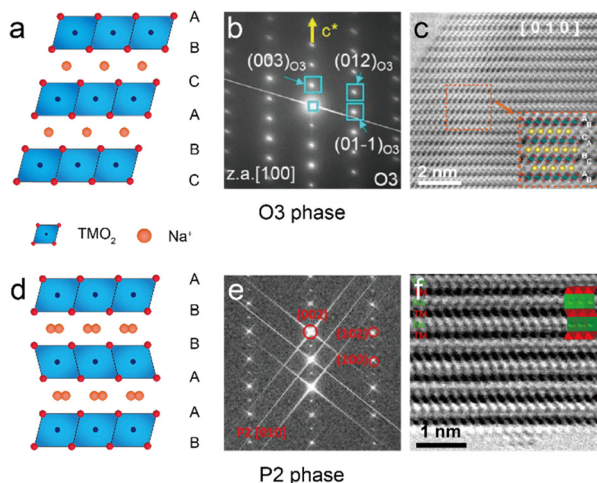
Fig. 2 (a) Crystal model of the O3 phase with three stacking TMO$_2$ layers. (b) SAED pattern of the O3 phase along the [100] axis. Reproduced with permission from ref. 21, copyright 2020 Wiley. (c) STEM-ABF image of a typical O3 phase Na$_{0.93}$Li$_{0.12}$Ni$_{0.25}$Fe$_{0.15}$Mn$_{0.48}$O$_2$ cathode along the [010] axis, with corresponding models shown in the inset. Reproduced with permission from ref. 22, copyright 2022 Wiley. (d) Crystal model of the P2 phase with two stacking TMO$_2$ layers. (e) SAED pattern of the P2 phase along the [010] axis. Reproduced with permission from ref. 24, copyright 2021 Wiley. (f) STEM-ABF image of a typical P2 phase Na$_{45/54}$Li$_{4/54}$Ni$_{16/54}$Mn$_{34/54}$O$_2$ cathode along the [010] axis, with corresponding models shown in the inset. Reproduced with permission from ref. 25, copyright 2020 American Chemical Society.

TMO$_6$ octahedral layers, while Na$^+$ ions reside between neighboring layers.[19] Fig. 2(a) and (d) show the two typical crystal structures of Na$_x$TMO$_2$: P2-type ($0.3 < x < 0.7$) and O3-type ($0.7 < x < 1$), based on the coordination environment of Na$^+$ ions and the stacking arrangement of O layers.[20] In O3-Na$_x$TMO$_2$ Na$^+$ ions are initially positioned at octahedral sites in an edge-sharing configuration, marked by an ABCABC oxygen sequence. The SAED pattern in Fig. 2b clearly shows the stacking ordering along the [100] axis.[21] In the STEM-ABF image, the oxygen atoms are visible in TMO$_2$ layers, aligning well with the crystal model.[22] For P2-Na$_x$TMO$_2$, Na$^+$ ions are initially situated at trigonal prismatic locations, either arranged in an edge-sharing or face-sharing configuration, characterized by an ABBA oxygen sequence.[23] The corresponding SAED patterns and ABF images of a P2-Na$_x$TMO$_2$ sample viewed at the [010] orientation are shown in Fig. 2e and f, where the TM slab and Na$^+$ ion slab stacking is visible in the ABF image.[24,25] The two examples clearly display the atomic structures of P2- and O3-Na$_x$TMO$_2$ materials directly by STEM imaging techniques.

Apart from the two typical phases, other types of layered oxides are also studied by TEM imaging techniques. P3 phase layered oxides are reported as long-life and high-rate SIB cathode materials. Song *et al.* applied high-resolution TEM to investigate the P3 ordering of their Na$_{0.48}$Ni$_{0.2}$Mn$_{0.8}$O$_2$ cathode.[26] Moreover, Sambandam *et al.* used SAED to distinguish the P3- and P2-phases of samples and measured the *d* spacing for the two samples.[27] Another type of layered oxide, the O2 phase, commonly appears at the charging state of the P2

phase due to an oxygen framework shift.[28] Wang *et al.* observed the O2 phases using STEM ABF and HAADF images, confirming the P2–O2 phase transition.[29]

3.2 Superlattices and heterostructures

Superlattice structure is investigated by introducing external ions into TM layers to form periodical orders. The doped ions and original TM ions are arranged along the [100] direction to build up a structured pattern. A good example is shown in Fig. 3(a). Wang *et al.* introduced Sb into the typical NaNiO$_2$ system to form a highly stabilized phase with a honeycomb superlattice structure in the Na[Ni$_{2/3}$Sb$_{1/3}$]O$_2$ cathode.[30] In the STEM-HAADF image, the Sb and Ni ions are marked by larger and smaller bright spots along the [100] zone axis, with the sequence of Sb–Ni–Ni–Sb. The O ions are visible in the STEM-ABF image on both sides of the Ni/Sb layers, and some vanished O columns suggest the stacking faults in lateral displacements. Such Ni$_6$-rings form a symmetric atomic configuration thus degenerating the electronic orbitals. The rigid framework
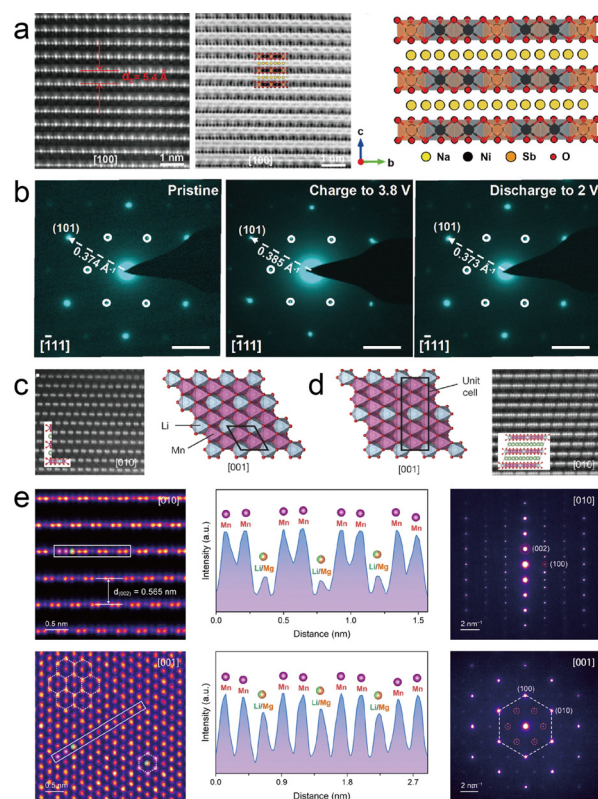

Fig. 3 (a) STEM-HAADF and ABF images of the Ni$_6$-ring ordered Na[Ni$_{2/3}$Sb$_{1/3}$]O$_2$ cathode. Reproduced with permission from ref. 30, copyright 2019 Wiley. (b) *Ex situ* SAED patterns of the Na(Ni$_{2/3}$Ru$_{1/3}$)O$_2$ cathode in the pristine state, charged to 3.8 V, and discharged to 2 V, respectively. Reproduced with permission from ref. 31, copyright 2020 Wiley. (c) Designed honeycomb superlattice of the Na$_{0.75}$[Li$_{0.25}$Mn$_{0.75}$]O$_2$ cathode and (d) ribbon superlattice structure of the Na$_{0.6}$[Li$_{0.2}$Mn$_{0.8}$]O$_2$ cathode. Reproduced with permission from ref. 36, copyright 2020 Springer Nature. (e) STEM-HAADF images with corresponding SAED patterns of the Li/Mg dual-site substituted Na$_{0.7}$Li$_{0.03}$[Mg$_{0.15}$Li$_{0.07}$Mn$_{0.75}$]O$_2$ cathode along the [010] and [001] axes, respectively. Reproduced with permission of ref. 38, copyright 2023 American Chemical Society.

ensures the transportation tunnels of Na^+ ions and enhances both the cycling stability and air sensitivity. Zhou *et al.* proposed a Ni$_6$–Ru honeycomb superlattice Na(Ni$_{2/3}$Ru$_{1/3}$)O$_2$ cathode, in which the interactive force generated by the regular TM arrangement maintains the system structure and ensures the high-stability of TM layers during desodiation and sodiation. By applying *ex situ* SAED, the cathode particle is found to hold the superlattice diffraction patterns, and the spacing between TM layers indicates the breathing of the crystal lattice during Na^+ release and uptake, as shown in Fig. 3(b).[31] Such SAED techniques are suitable to confirm the superlattice structure during charging/discharging states of single cathode particles, especially for the designed ordering of TM ions. Similar design strategies of the Ni$_6$ structure can also be found in ref. 32–35.

In addition to the external TM ion substitution, Li^+ ions are also well studied to periodically replace the TM sites in layer oxides. Peter *et al.* reported that the local ordering of Li^+ and TM ions determines the 1st-cycle voltage hysteresis.[36] The honeycomb and ribbon superlattice structures were studied by advanced TEM, as shown in Fig. 3(b) and (c). Due to the contrast, the Li^+ columns are hardly visible in the STEM-HAADF images. Nevertheless, the ordering of Li^+:TM = 1:2 can be clearly seen in Fig. 3(c), while the ribbon-structure shows an ordering of Li^+:TM = 1:4 in Fig. 3(d). By comparing the structural evolution during charge/discharge, the honeycomb superlattice disappears in the charging state partially due to the formation of molecular O$_2$. In comparison, the ribbon structure can be observed in the charging state, indicating the suppression of O$_2$ and inhibition of the voltage hysteresis. Based on this, Gu *et al.* reported a topological structure in a P3-Na$_{0.6}$-Li$_{0.2}$Mn$_{0.8}$O$_2$ cathode which has a high capacity of 240 mA h g^{-1} with outstanding cycling stability. Its structure on cycling undergoes reversible evolutions due to the initial stackings. In comparison, the stacking in the P2-Na$_{0.6}$Li$_{0.2}$Mn$_{0.8}$O$_2$ cathode totally changed after 10 cycles. Such changes are clearly visible in atomic-resolution STEM-HAADF images. Different from the reported single-site superlattice structure, Zhou *et al.* constructed a dual-site honeycomb superlattice cathode in which the Li$_6$-Mn rings along with Mg$_6$-Mn rings are formed in TM slabs.[37] The dual-honeycomb strategy can simultaneously realize high activity and reversibility of lattice O redox. A Li/Mg dual-site substituted Na$_{0.7}$Li$_{0.03}$[Mg$_{0.15}$Li$_{0.07}$Mn$_{0.75}$]O$_2$ cathode was also reported by Chen *et al.*, as shown in Fig. 3(e).[38] The STEM-HAADF images clearly show the Li/Mg–Mn–Mn–Li/Mg ordering along the [010] axis and a direct view of the honeycomb structure along the [001] zone axis, which is confirmed by the line profiles, respectively. The corresponding SAED patterns indicate the phase purity and hexagonal lattice symmetry.

Compared to single-phase layered oxide, heterostructure Na$_x$TMO$_2$ has gained much interest. A heterostructure is defined by the integration of two phases with a shared interface. Major promising heterostructures include P2/O3, O3/P3, and P2/P3 combinations, with specific advantages for each.[39–45] Local distortions at the interface can generate an electric field
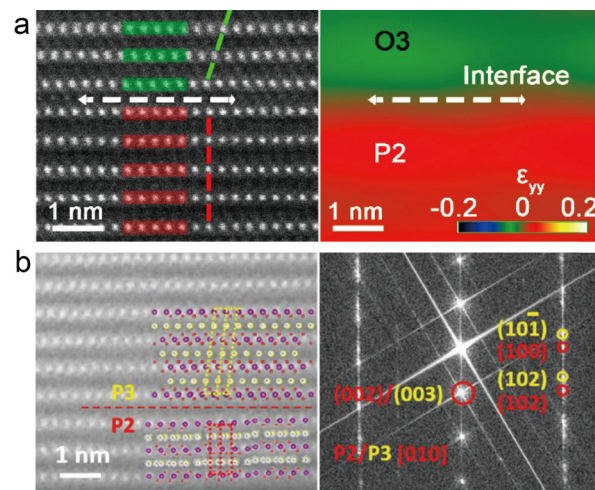

Fig. 4 (a) STEM-HAADF image of the O3/P2 hybrid composite of the O3/P2 a$_{0.8}$[Ni$_{0.5}$Co$_{0.2}$Mn$_{0.3}$]O$_2$/Na$_{0.8}$[Ni$_{0.33}$Mn$_{0.67}$]O$_2$ cathode with corresponding strain mapping. Reproduced with permission from ref. 50, copyright 2020 American Chemical Society. (b) STEM-HAADF image of a P2/P3 biaphase Na$_{0.67}$Mn$_{0.64}$Co$_{0.30}$Al$_{0.06}$O$_2$ particle with corresponding FFT patterns. Reproduced with permission of ref. 41, copyright 2021 Wiley.

that activates new Na^+ storage sites and accelerates the transportation of ions and electrons.[46] Moreover, the chemomechanical coupling and micro-strain due to the interfacial bonding greatly enhance the mechanical integrity of layered oxides.[47] Such hybrid structural composites of O- and P-phases have been proven to effectively improve the electrochemical performance of SIBs.[48,49] The heterostructure composite cathodes can be distinguished by SAED with featured patterns. More precise characterization can be carried out using the atomic scale STEM-HAADF images. Chen *et al.* reported their study of a core–shell structure layered oxide consisting of O3-Na$_{0.8}$[Ni$_{0.5}$Co$_{0.2}$Mn$_{0.3}$]O$_2$ and P2-Na$_{0.8}$[Ni$_{0.33}$Mn$_{0.67}$]O$_2$.[50] The STEM-HAADF image shown in Fig. 4(a) demonstrates a coherent P2/O3 intergrowth structure, and the geometric phase analysis (GPA) analysis is conducted to identify the phase boundary and strain mapping. The coherent interface is shown with uniform strain distribution, indicating sufficient channels for Na^+ transportation during cycles. Jiang *et al.* introduced Co into layered Na$_x$MnO$_2$ to get a P2/P3 biphasic cathode material, Na$_{0.67}$Mn$_{0.64}$Co$_{0.30}$Al$_{0.06}$O$_2$.[41] As shown in Fig. 4(b), the P3- and P2-phases share a Na slab with small lattice distortions at the near-interface area. The corresponding fast-Fourier transformation (FFT) patterns viewed along the [010] direction are highly consistent with the intergrowth of P2/P3 biphases.

3.3 High-entropy cathodes

The high-entropy (HE) strategy is one of the most promising approaches to obtain higher specific capacity and long cycle life in layered oxides.[51–53] HE oxides are defined by the combination of five or more different cations in a single-phase layered oxide with equal atomic ratios and finally reaching a high configuration entropy.[54] In the SIB system, HE layered oxides have the advantages of outstanding ionic conductivity and

strong structural stability.[55–57] The introduction of appropriate elements into the TMO_2 slabs has been demonstrated as an effective solution for the distinct challenges in SIBs, such as poor cycling stability derived from phase transitions, lattice distortions induced by the Jahn–Teller effect, and structural irreversibility due to oxygen redox.[58–63] With more elements substituted into HE layered oxides, the position or distribution of each element has a sequential impact to hold a stable lattice system. Inductively coupled plasma (ICP) spectroscopy can determine the chemical compositions on a large scale but the locations are still unknown. STEM-EDS and EFTEM can map the elemental distribution on both micro- and nanometer scales. Elemental mapping has become an indispensable method for determining the stoichiometry in HE oxides. Fig. 5(a) shows the EDS mapping of the $Na_{0.95}Li_{0.06}Ni_{0.25}Cu_{0.05}Fe_{0.15}Mn_{0.49}O_2$ cathode for each TM ion (Ni, Cu, Fe, and Mn).[64] And the line profile confirms the uniform distribution at atomic resolution in the designed HE oxides.

As discussed, the good arrangement of various TM ions leads to better lattice stability and structural integrity of layered oxides.[65,66] Huang *et al.* performed GPA analysis of $Na_{0.95}Li_{0.05}Mg_{0.05}Cu_{0.20}Fe_{0.22}Mn_{0.35}Ti_{0.13}O_2$ (HE-CFMO) and bare $Na_{0.95}Mg_{0.05}Cu_{0.20}Fe_{0.35}Mn_{0.40}O_2$ (CFMO) cathodes to estimate the internal strains at atomic resolution.[67] Fig. 5(b) shows the STEM-HAADF images along with corresponding atomic strain distribution mapping of HE-CFMO and CFMO samples. The tensile strains (in red) are visible in both samples along the ε_{xx} dimension. The in-homogeneous linear patterns in the CFMO cathode demonstrate the uneven expanding stress and more aggressive strain distributions appear in the ε_{xy} and ε_{yy} dimensions, indicating an unstable lattice structure. In comparison, the tensile and compression strains are more uniform among

all dimensions in HE-CFMO. The GPA analysis of HE and normal layered oxides confirms the lattice stability of the HE strategy. The GPA analysis was also applied by Yan *et al.* to compare the microstructure evolution of $NaLi_{0.1}Ni_{0.15}Cu_{0.1}Mg_{0.1}Ti_{0.2}Mn_{0.35}O_2$ and $NaLi_{0.1}Ni_{0.35}Mn_{0.55}O_2$ cathodes.[68] The HE sample shows a uniform strain distribution after discharge compared to the terrible mismatched strains for the original $NaLi_{0.1}Ni_{0.35}Mn_{0.55}O_2$ particle.

3.4 Surface modification

The layered oxide surface should be taken into consideration during the design and manufacturing due to the failure mechanisms induced by the cathode–electrolyte interface erosion and dissolution of transition metals. Apart from constructing composite phases or core–shell structures, the coating layer can also effectively suppress the material failure during the cycling.[69–71] Recently, gradient surfaces by various ion doping have attracted much attention. Luo *et al.* reported a gradient Mg^{2+} doping surface on the $Na_{0.67}Mn_{0.67}Ni_{0.33}O_2$ cathode and achieved high specific capacity and good cycling stability.[72] A further study on the gradient Mg^{2+} doping was proposed by Jiang *et al.*[73] The gradient surface strategy is applied on the $P2-Na_{0.72}Ni_{0.20}Co_{0.21}Mn_{0.55}Mg_{0.036}O_2$ cathode with Mg content increasing from the interior to the shell's outer surface. As shown in Fig. 6(a), a lamella is prepared of a secondary spherical particle, and the core and the shell structures are revealed by the STEM-HAADF images. No bright spots are visible in Na slabs, indicating the Mg^{2+} ions are substituted into the TMO_2 layers. The layer spacings of the core and shell are 5.55 and 5.52 Å, respectively, similar to the lattice distance of the typical $Na_{0.72}Ni_{0.2}Co_{0.25}Mn_{0.55}O_2$ particle. Moreover, the TM valence states are studied by EELS, as shown in Fig. 6(b). It is obvious that the peaks of Ni-edges shift to lower energy, indicating the decrease of the Ni valence from the shell to core region, while there are no apparent shifts in the peaks of Mn-edges and Co-edges. The valence change is consistent with the
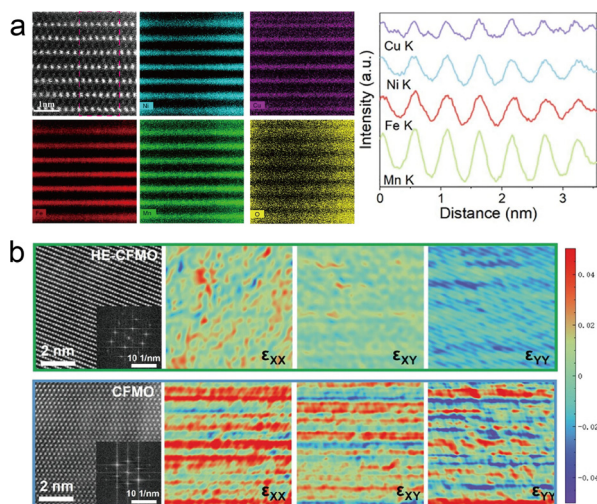
Fig. 5 (a) STEM-EDS mapping of O and TM elements, Ni (cyan), Cu (purple), Fe (red), and Mn (green) of the HE layered oxide $Na_{0.95}Li_{0.06}Ni_{0.25}Cu_{0.05}Fe_{0.15}Mn_{0.49}O_2$, with corresponding line profiles across the layers. Reproduced with permission from ref. 64, copyright 2023 Springer Nature. (b) STEM-HAADF images and the corresponding GPA analysis results of HE-CFMO and CFMO cathodes. Reproduced with permission from ref. 64, copyright 2024 Wiley.
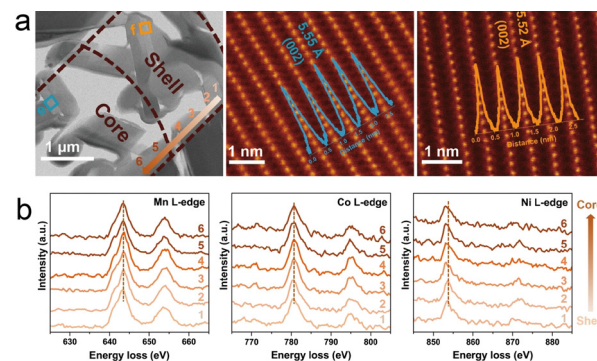
Fig. 6 (a) STEM-HAADF image of a lamella including the shell and the core of the secondary spherical particle prepared by focused ion beam. The corresponding STEM-HAADF images of core and shell structures are also presented with line profiles showing the layer spacing. (b) The representative EELS spectra of Mn L-edge, Co L-edge, and Ni L-edge. The line scan direction and acquisition position are marked by the orange arrow and numbers in (a). Adapted with permission from ref. 73, copyright 2024 Wiley.

Feature Article

ChemComm

View Article Online

substitution of low-valence Mg for charge neutrality. The results confirm the gradient Mg^{2+} surface and ensure such a strategy can suppress the irreversible phase transition in the P2-type cathode.

4. Structural evolution

4.1 Phase transition

Phase transition has been widely studied and reported in layered oxides.[74–77] Most O3-phase Na_xTMO_2 cathodes experience O3–P3 phase transition during the charging process. Such a phase transformation occurs in order to reduce the system energy with the extraction of Na^+ ions. It should be noted that more complex phase transitions would appear beyond cutoff voltage, such as O3–O1–P3–P1 phase transition in $O3-NaNi_{1/3}Mn_{1/3}Co_{1/3}O_2$.[78] *In* or *ex situ* XRD can distinguish the different phases in the charging/discharging process. However, the distribution of various phases in particles requires a more precise study. Zhang *et al.* reported a good example of the combination of XRD and TEM to show the O3–P3–OP2 phase transitions.[79] In the typical $O3-Na_{0.9}Ni_{0.4}Fe_{0.1}Mn_{0.5}O_2$ cathode, the (003) and (006) peaks in the XRD pattern shift to lower angles when charging, while the OP2 phase appears when charged over 3.6 V. Such a P/O phase transition is investigated through STEM-HAADF images, and the spacing between TM slabs increased from 5.4 Å (pristine) to 5.7 Å (charged to 3.6 V). Yao *et al.* reported another complex O3–P3 phase transition in the $Na_{2/3}Li_{1/6}Fe_{1/6}Co_{1/6}Ni_{1/6}Mn_{1/3}O_2$ cathode, as shown in Fig. 7(a).[80] From the XRD results, the pristine O3 phase is transformed into the P3 phase (charged to 3.0 V), a new O3 phase, and the P3 phase (charged to 4.5 V), and finally recovered to the O3 phase when discharged to 2.0 V. The co-existence of the P3 + O3 phase sequence is defined but it is unknown from *in situ* XRD how the two phases exist in particles at the nanoscale. By applying STEM-HAADF, the interlayer structure of O3 + P3 is clearly shown when charged to 4.5 V. The atomic structure indicates that the high-entropy strategy greatly enhances the stabilization among layers.

For $P2-Na_xTMO_2$ cathodes, P2–O2 phase transition occurs during the charging process, including the biphase-coexisting structure (P2 + O2).[82,83] Recent studies show a so-called OP4 phase in various P2-phase layered oxides when charging to high voltages.[84–86] Based on these reports, Wang *et al.* studied the content of O- and P-phases at different charging states.[81] As shown in Fig. 7(b), the $P2-Na_{0.67}Li_{0.1}Fe_{0.37}Mn_{0.53}O_2$ cathode is firstly charged to 4.3 V and 4.5 V, then characterized by the STEM-HAADF, and the P/O phase ratio is determined. When charging to 4.3 V, the P phases dominate the OP4 structure, while more O-type layers and obvious neighbouring O-type stacking appear when charged to 4.5 V. Such evolution indicates the O/P interlayer structure evolves from a P-type rich state to an O-type rich state with extraction of more Na^+ ions. Similar findings of the P-to-O phase transition are also reported.[87]
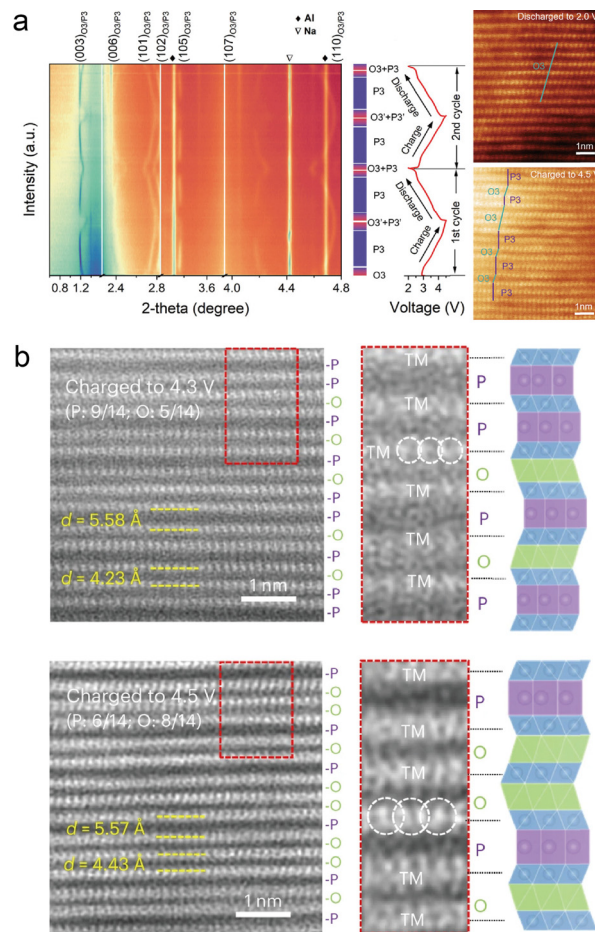

Fig. 7 (a) *In situ* XRD and corresponding STEM-HAADF images of the $Na_{2/3}Li_{1/6}Fe_{1/6}Co_{1/6}Ni_{1/6}Mn_{1/3}O_2$ cathode when charging to 4.5 V and discharging to 2.0 V, respectively. Reproduced with permission from ref. 80, copyright 2022 Wiley. (b) STEM-HAADF images of the $Na_{0.67}Li_{0.1}Fe_{0.37}Mn_{0.53}O_2$ cathode at 4.3 V and 4.5 V charging states, respectively. Reproduced with permission from ref. 81, copyright 2024 Springer Nature.

4.2 Surface evolution

The microstructure evolution of layered oxides preferentially occurs on the surface area of a single particle due to the direct contact between the cathode and electrolyte. Under long-term Na^+ transportation and possible invasion of a liquid electrolyte, the surface could be damaged with numerous dislocations, cracks along layers, and a severe TM–Na mixing rock-salt phase.[88,89] Ding *et al.* studied the planar strain in a layered oxide, and the STEM-HAADF results of the $NaNi_{0.3}Cu_{0.1}Fe_{0.2}Mn_{0.3}Sn_{0.1}O_2$ particle are shown in Fig. 8(a).[90] One could see the intragranular cracking in a single particle, and the surface is also visible at the atomic scale, including plenty of lattice dislocations and rock-salt phases. The Na^+ transportation tunnels are blocked due to the damaged surface, thus leading to the degradation of electrochemical performance. TM dissolution could simultaneously occur with the surface evolution, for example, Mn-based layered oxides which suffer from the Jahn–Teller effect.[91–93] To suppress the voltage decay and reduce surface damage, Sun *et al.* introduced Al^{3+} ions
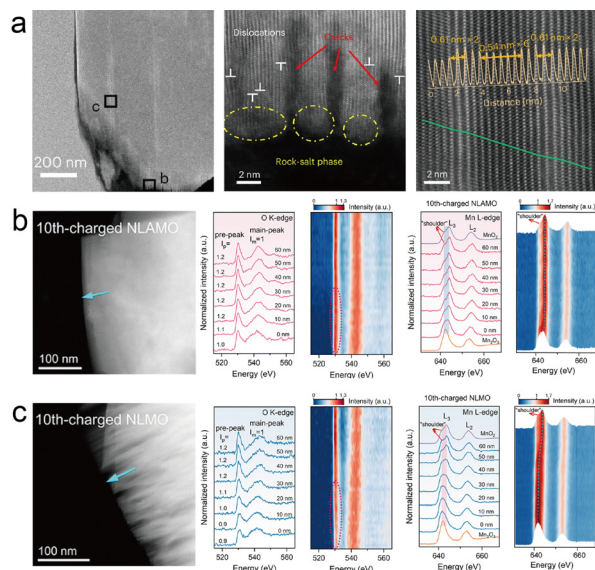
Fig. 8 (a) Cross-sectional STEM-HAADF image of the $NaNi_{0.3}Cu_{0.1}$-$Fe_{0.2}Mn_{0.3}Sn_{0.1}O_2$ particle after 500 cycles, with enlarged HAADF images showing the substantial dislocations, cracks, and rock-salt phases on the surface. Adapted with permission from ref. 90, copyright 2024 Springer Nature. (b) STEM-HAADF image of the $Na_{0.8}Li_{0.24}Al_{0.03}Mn_{0.73}O_2$ particle with intact surface. The EELS line profiles of O-edges and Mn L-edges are scanned from the bulk to surface. (c) STEM-HAADF image of the $Na_{0.8}Li_{0.24}Mn_{0.76}O_2$ particle with a damaged surface. The EELS line profiles of O-edges and Mn L-edges are scanned from the bulk to surface. Adapted with permission from ref. 94, copyright 2024 Royal Society of Chemistry.

into P2-type layered oxide and designed a $Na_{0.8}Li_{0.24}Al_{0.03}$-$Mn_{0.73}O_2$ cathode to achieve effectively restrained oxygen release and it outputs highly stable voltage within 200 cycles.[94] The surface area is highlighted with original $Na_{0.8}Li_{0.24}Mn_{0.76}O_2$ cathodes. The STEM-HAADF image Fig. 8(b) shows an intact surface of the $Na_{0.8}Li_{0.24}Al_{0.03}Mn_{0.73}O_2$ particle after 10 cycles. The EELS profile of unchanged peak intensity in O K-edges and Mn L-edges demonstrates the improved lattice oxygen stability and structural integrity during electrochemical cycling. In contrast, the surface of $Na_{0.8}Li_{0.24}Mn_{0.76}O_2$ particles gets ruined with multi intragranular cracks (see Fig. 8(c)). The EELS profile of O K-edges reveals the O vacancy formation in the 40-nm region from the surface, which is mainly caused by the irreversible oxygen redox. The chemical shift in Mn L-edges indicates the valence change on the surface, and more Mn^{3+} are located at around 40 nm from the surface, leading to severe Mn^{3+} dissolution after long-term cycling. By using STEM-HAADF imaging and EELS analysis, the strong bonding from Al^{3+} substitution can be confirmed. More examples of surface evolution monitored by such advanced TEM techniques can be found in ref. 95–97.

5. Failure analysis

When focusing on battery failure, the most critical drawback of Na_xTMO_2 cathodes is the multi-phase transitions during the

charge/discharge process, which are mainly manifested in the form of multi-voltage plateaus in voltage–capacity profiles.[75,98,99] The poor Na^+ ion transportation kinetics would lead to the instability of the cathode structure, further plaguing the cycling performance.[100] Repeated Na^+ ion insertion/extraction would lead to interlayer inhomogeneous strain and finally cause degradation. For SIBs, the failure mechanisms mainly relate to layer gliding, cracking, and cation migration.

5.1 Layer gliding

The gliding of neighbouring layers mainly occurs due to the electrostatic repulsion of lattice oxygen or vacancies of Na depletion in the charge/discharging process.[101,102] Layer gliding leads to the transitions of stacking types and sequences, reaching a more energetically stable state.[103] The process is revisable in most cases, but the strain in the phase boundaries could easily accumulate due to the sudden and drastic volume changes, finally triggering deterioration. Apart from the planar gliding in layer oxides, Li *et al.* reported a new type of degradation mechanism by kinking in a P-$Na_{0.7}Ni_{0.3}Mn_{0.6}Co_{0.1}O_2$ cathode using *in situ* TEM techniques.[104] As shown in Fig. 9(a), the STEM-HAADF image shows a narrowly kinked region within 10 interconnected TMO_6 octahedra in each TMO_2 slab, while the STEM-ABF image shows the Na^+ ions between the adjacent TMO_2 slabs which are not altered by the bending formation. Fig. 9(b) shows the two modes of bending by either planar strain or interlayer slipping. By counting the number of TMO_6 octahedra, the interlayer gliding has occurred in the kinked area. Such large bending is further tested by the *in situ* mechanical compression experiment using TEM. The similar kink
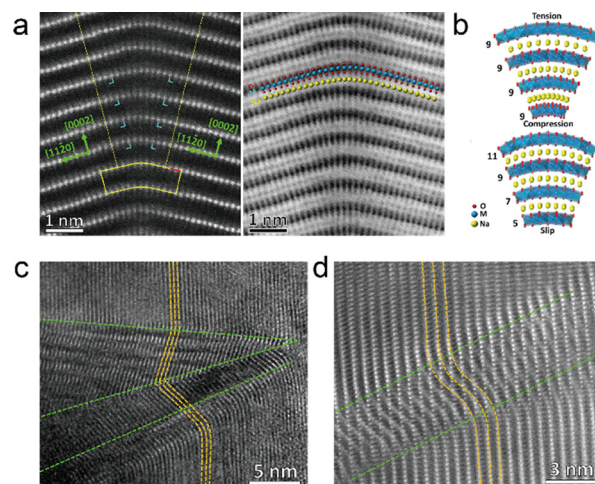

Fig. 9 (a) STEM-HAADF and ABF images viewed along the $[1\bar{1}0]$ direction, showing the kinked MO_2 layers. Large white dots correspond to transition metal ions. The kinked region (delimited by the two yellow dashed lines) consists of an array of dislocations stacked vertically one above another. (b) Structural models of the bending by in-plane tensile/compressive strain of TMO_2 layers and interlayer slip. (c) HRTEM image shows kink information after compression. (d) STEM-HAADF image shows lattice fringes overlapping those of the non-kinked part, forming Moiré fringes in the overlapped regions (marked by green dashed lines). Adapted with permission from ref. 104, copyright 2021 American Chemical Society.

regions shown in Fig. 9(c) and (d) suggest that bending and kinking are the primary mechanisms of plastic deformation. A localized, nonuniform interlayer slip leads to kink formation, whereas a delocalized, uniform interlayer slip results in phase transformation in layered oxides.

5.2 Cation migration

During the Na^+ ion extraction process, the TM ions could migrate to Na slabs to occupy the vacancies. This phenomenon is earlier found in LIBs, known as cation disorder or cation migration, due to the similar ionic radius of alkali ions and TM ions.[105,106] The migration is normally considered irreversible and causes large unexpected capacity fading and structural deterioration upon cycling. Talaie et al. applied operando XRD combined with atomic pair distribution function technique to investigate the possible cation migration in the P2-type $Na_{2/3}[Mn_{1/2}Fe_{1/2}]O_2$ cathode.[107] Direct observation of reversible cation migration is proposed by Zhang et al. in the $Na_{0.8}Co_{0.4}Ti_{0.6}O_2$ cathode.[108] Fig. 10(a) shows the STEM-HAADF images at different states, pristine, charging, and discharging, along with the line profiles, respectively. It is clear to see the mixed bright

spots popping up among TMO_2 slabs at the charging state, and the line profile intensity confirms the strong cation/Na mixing. It is noteworthy that at the discharging state, the line profile shows a weak mixing at Na slabs, indicating the reversible cation migration. A similar study was reported by Chen et al. on the O3-type $NaNi_{0.3}Co_{0.12}Mn_{0.18}Fe_{0.4}O_2$ cathode.[109] STEM-HAADF and the corresponding line profiles shown in Fig. 10(b) indicate the cation migration and cause cation/Na mixing. Further work is carried out by EDS mapping at the atomic level, shown in Fig. 10(c). The EDS results confirm the spatial distribution of Mn and Co residing in TM slabs, while Ni and Fe are found in Na slabs. The intensity profiles of Fe and Ni reveal that the Fe element firstly migrates to Na slabs with the extraction of Na^+ ions and then the Ni element predominantly resides on the octahedral interstices of the Na layer after cycling. Their study shows the stability priority of these four TM ions in layered oxides, where Mn and Co ions are the most stable TM species.

5.3 Cracking

Cracking is another key factor influencing the electrochemical performance. It is commonly considered that the more complex phase transition at high-voltage charge leads to irreversible structural changes at bulk and huge volume changes.[110,111] These two conditions cause the mechanical stress accumulation at boundaries due to the lattice mismatch and further form intergranular or intragranular cracks in layered oxides.[89,112] In a typical $NaNi_{1/3}Fe_{1/3}Mn_{1/3}O_2$ cathode, Yang et al. observed the cracks and heavy surface decomposition at the surface by STEM-HAADF.[113] The structural degradation is attributed to the cation migration and phase transition. Wang et al.[66] reported P2-$Na_{2/3}Ni_{1/3}Mn_{2/3}O_2$ as an example to investigate the crack formation during high-voltage cycling. Large cracks are observed in single particles with atomic-resolution STEM-HAADF images showing the primary grains breaking down, as shown in Fig. 11(a). Corresponding EDS maps in Fig. 11(b) show that the crack areas are Na-depleted layers. The concentration of organic stuff, C and Cl elements, indicates the decomposition of electrolytes in cracks. Hence, the authors propose a stress corrosion cracking mechanism, as shown in Fig. 11(c). The strain built at the P2/O2 boundaries during the 1st P2–O2 transition could initialize crack nucleation. The crack tip propagates along the grain boundary into the bulk. In this area, Na^+ ions can be easily extracted and more TM ions migrate and dissolute into electrolytes. With the accumulation of surface corrosion and TM condensation, the small crack grows and expands, finally generating intragranular cracks.

One more detailed study on the cracking formation was carried out by Xu et al. showing that native lattice strain induces structural cracks.[114] As shown in Fig. 11(d), the HRTEM image of O3-$NaNi_{0.4}Mn_{0.4}Co_{0.2}O_2$ shows that the d spacing along the (003) zone axis is 0.549 nm, around 3.58% stretch compared to the standard O3 phase, and some severe lattice distortions are visible. Geometric phase analysis (GPA) shows a mismatch between the layer and strain directions. Such native lattice strain tends to stretch the lattice along the
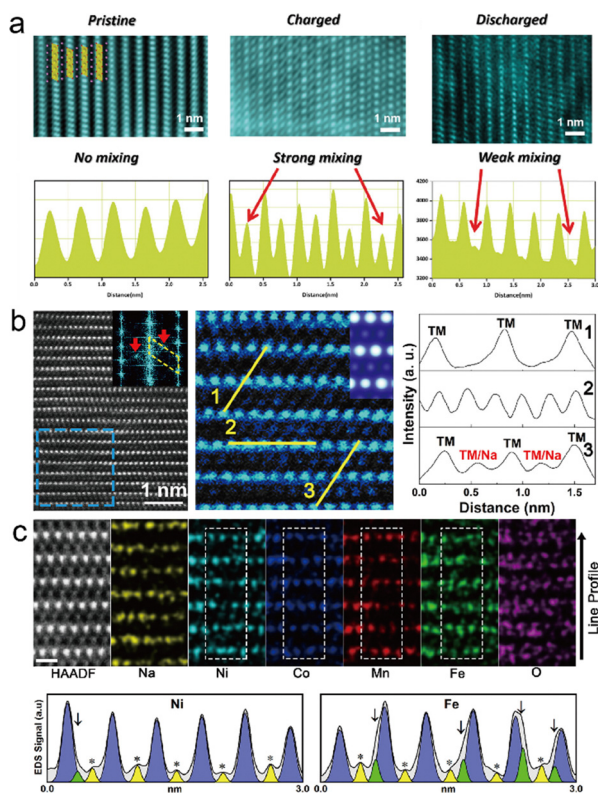

Fig. 10 (a) STEM-HAADF images and their corresponding line profiles of the $Na_{0.8}Co_{0.4}Ti_{0.6}O_2$ electrode at different stages, pristine, charging, and discharging, respectively. Reproduced with permission from ref. 108, copyright 2019 Wiley. (b) STEM-HAADF images of the $NaNi_{0.3}Co_{0.12}Mn_{0.18}Fe_{0.4}O_2$ cathode when charged to 4.0 V along the [100] zone axis, and the corresponding line profiles. (c) Atomic resolution EDS mapping after 50 cycles along the [100] zone axis and correspond line profile of Ni and Fe elements. Reproduced with permission from ref. 109, copyright 2020 American Chemical Society.
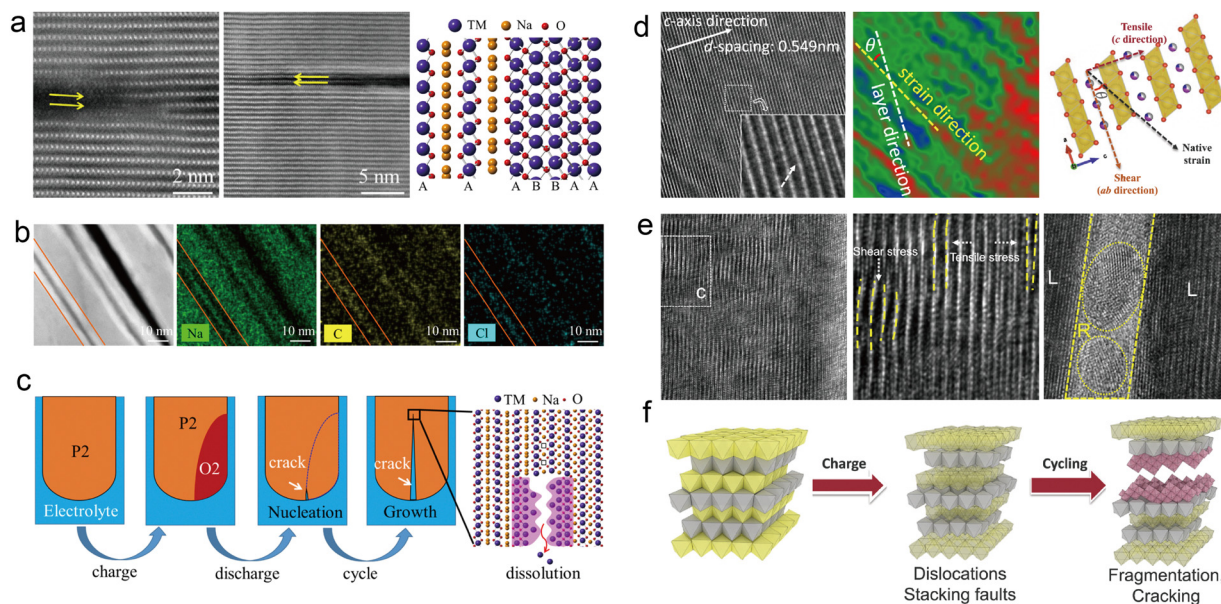
Fig. 11 Left half: (a) STEM-HAADF images of intragranular cracks in the $Na_{2/3}Ni_{1/3}Mn_{2/3}O_2$ cathode after 50 cycles with an atomic model. (b) EDS maps of Na, C, and Cl elements, demonstrating Na depletion on crack surfaces and electrolyte decomposition. (c) Schematic diagram showing crack's nucleation and growth. Adapted with permission from ref. 66, copyright 2018 Elsevier. Right half: (d) HRTEM image, GPA analysis and atomic structural model of the strained $NaNi_{0.4}Mn_{0.4}Co_{0.2}O_2$ cathode. (e) HRTEM images after 100 cycles in 2.0–4.4 V. (f) Schematic illustration of the structural fragmentation and cracking during cycling. Adapted with permission of ref. 114, copyright 2022 Springer Nature.

c axis and shear stress along a and b axes to compress the lattice. After 100 cycles in 2.0–4.4 V, the stacking faults and dislocations appear in the $NaNi_{0.4}Mn_{0.4}Co_{0.2}O_2$ cathode as a consequence of strain relaxation. The bending lattice parallel to the layers and the tensile lattice along the c axis can be clearly seen. Simultaneously, the intrinsic high lattice strain in the quenched cathode significantly exceeds the tensile and compressive limits of the rock-salt phase, resulting in the formation of rock-salt fragments with varied orientations. Such high-strained structural evolution is illustrated in Fig. 11(f). The degradation in layered oxides originates from the spontaneous relaxation of internal strain that exceeds the threshold limit.

5.4 Instability in air

A critical challenge for layered oxide Na_xTMO_2 is the rapid degradation once exposed to air for several hours, which could lead to capacity loss and reduced cycle life.[115] Several degradation models have been proposed to explain the possible reactions after air exposure.[116,117] Zuo et al. studied structural transformation of P2-type $Na_{0.67}MnO_2$ and $Na_{0.67}Ni_{0.33}Mn_{0.67}O_2$ in humid air and expanded their findings to the Mn-based layered oxides.[118] To figure out the formation on the surface after air exposure, the $Na_{0.67}MnO_2$ and $Na_{0.67}Ni_{0.33}Mn_{0.67}O_2$ particles are characterized by STEM-EDS mapping as shown in Fig. 12(a) and (b), respectively. The cracks on the surface of the exposed $Na_{0.67}MnO_2$ particle can be clearly seen, and the concentrations of O, C, and Na elements are visible at the surface extension part without Mn. The $NaHCO_3$ formation is also observed in the $Na_{0.67}Ni_{0.33}Mn_{0.67}O_2$ particles after being exposed to humid air (93% relative humidity + CO_2

atmosphere). It is concluded that the resistance to air of P2-type layered oxides highly depends on the redox potential properties in the 1st charge process. A further exploration was proposed in recent days by Yang and co-workers.[119] The O3-$NaNi_{1/3}Fe_{1/3}Mn_{1/3}O_2$ cathode is selected as the model system to study the structural evolution in different atmospheres. The lattice dislocations, expansion, and intragranular cracks can be clearly seen after 12 h-exposure to CO_2 with water vapor, with several atomic layer reconstructions on the surface, as shown in Fig. 12(c). When exposed to O_2 with water vapor even for 48 hours, the surface reconstructions occur without any lattice distortions or cracks. Once exposed to air for 48 hours, the lattice gets curvatures with a fraction of amorphized areas on the surface. To corroborate the damaging effect of combined water vapor and CO_2, in situ EFTEM was performed to track the real-time structural changes. Fig. 12(d) shows the amorphous layer formation after 1 h exposure, and the lattice spacing expands from 5.33 Å to 5.40 Å. By using SAED, the structure of amorphous formation is defined to be $NaHCO_3$. The results coupled with other analysis results illustrate the air sensitivity mechanisms in layered oxides.

6. Outlook and perspectives

Owing to the development of advanced TEM techniques, significant breakthroughs have been made in unravelling the scientific mechanisms underlying electrochemical rechargeable batteries, especially SIBs. We summarize applications of TEM techniques, including high-resolution imaging, spectroscopy, and current in situ technologies, for studying layered TM oxides
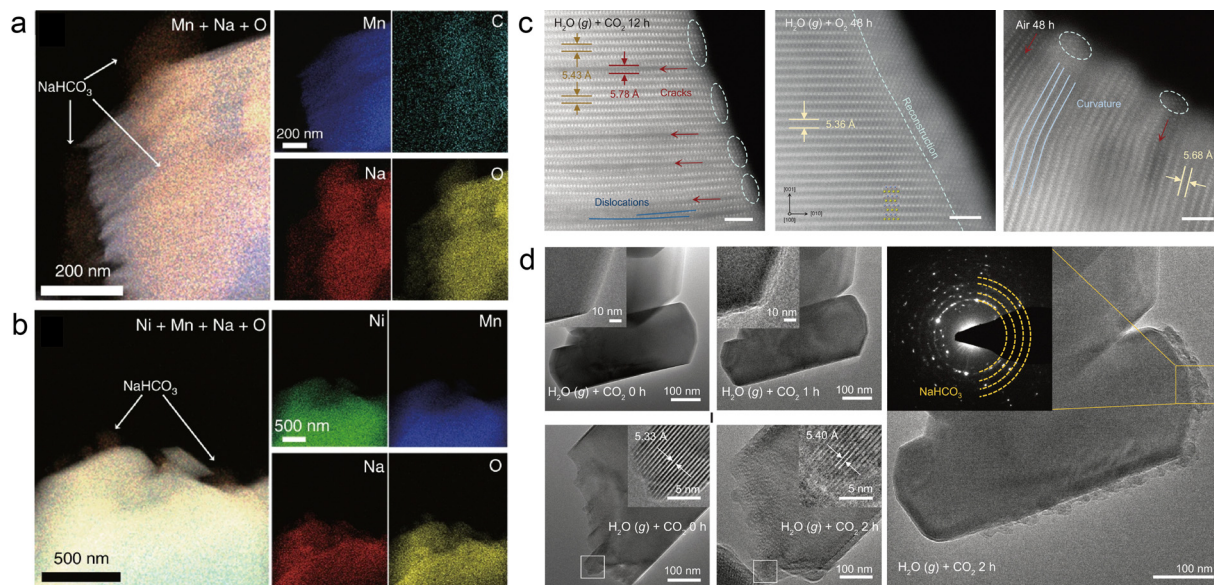
Fig. 12 Left half: (a) STEM–EDS maps of the exposed $Na_{0.67}MnO_2$ cathode, indicating the formation of $NaHCO_3$ the surface. (b) STEM–EDS mapping of humid air exposed $Na_{0.67}Ni_{0.33}Mn_{0.67}O_2$ particles. $NaHCO_3$ particles are also observed on the surface. Adapted with permission from ref. 118, copyright 2020 Springer Nature. Right half: (c) atomic STEM–HAADF images of the $NaNi_{1/3}Fe_{1/3}Mn_{1/3}O_2$ particle exposed to water vapor and a CO_2 atmosphere, demonstrating the damaged surface, including lattice dislocations, cracks, surface phase reconstruction, lattice expansion, and lattice curvature formation. (d) *In situ* TEM images of the $NaNi_{1/3}Fe_{1/3}Mn_{1/3}O_2$ particle exposed to water vapor and CO_2 to track the surface evolution. Adapted with permission from ref. 119, copyright 2024 AAAS.

for SIB cathodes. HRTEM and SAED modes are commonly employed for microstructure and spacing analysis of layered oxides. STEM-HAADF and -ABF imaging modes reveal atomic structures in pristine particles, capturing phase evolution and crack formation. Combined with spectroscopy instruments, EDS and EELS enable atomic-resolution tracking of elemental distributions, TM valence changes, and O status simultaneously. *In situ* TEM holders provide the SIB nature within the TEM column, allowing real-time observations of structure changes and the formation of CEIs. These techniques provide valuable insights into sodium ion intercalation and deintercalation, elucidating the principles of phase change and structural evolution in cathode materials. Additionally, they underscore the significance of ion doping and surface modification. Through the combined application of multiple TEM technologies, it has become evident that composite structure design, specific
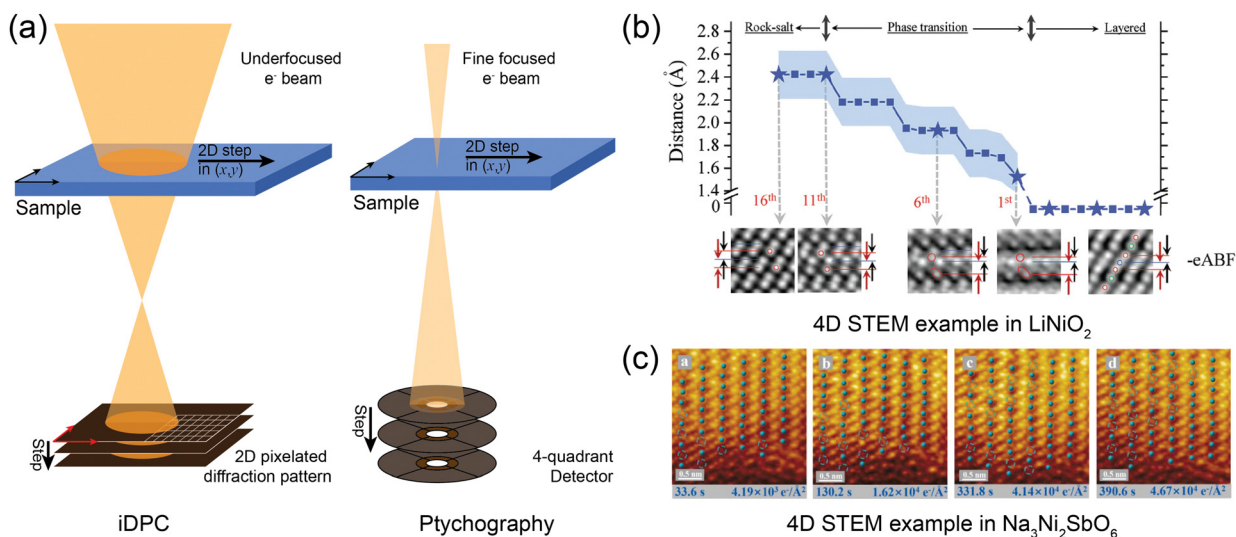

Fig. 13 (a) Schematic figures of major 4D STEM optics, iDPC and ptychography. (b) An example of 4D STEM applied in the $LiNiO_2$ cathode to track the phase transition and atomic distance. Reproduced with permission from ref. 123, copyright 2020 Wiley. (c) An example of 4D STEM used for studying layered oxides for SIBs, and the $Na_3Ni_2SbO_6$ cathode to visualize the Na vacancy formation under low ion doses. Reproduced with permission from ref. 126, copyright 2024 Elsevier.

phase change, cation doping and implantation, and surface modification play essential roles in energy storage performance. Engineering the Na^+ ion transport pathways of current cathode materials at the atomic scale by combining materials with different properties and implementing appropriate atomic doping to tune the electronic structure, along with other more direct methods, may present a feasible approach to overcome traditional cathode charge storage limitations.

The four-dimensional STEM (4D STEM) technique has been well studied and gradually applied to battery cathode materials. In this mode, the electron beam is focused and scanned over the sample, and the transmitted electrons with interaction information are collected by a pixelated detector at each probe position, as shown in Fig. 13(a). 4D consists of two data sets: two real-space dimensions of the scanning plane and two dimensions recording the diffraction information of scattered electrons at each probing position. The initial scattering information of electron-sample interactions is preserved in detail in the dataset. A key application of 4D-STEM is called ptychography, which reconstructs a specimen's structure by deriving its transmission function from convergent-beam electron diffraction patterns.[120–122] The imaging of 4D STEM allows a large beam scanning over the sample, which is beneficial for the beam-sensitive samples in layered oxides. The light-elements, such as O, and Na vacancies can be revealed by 4D STEM imaging, leading to a more precise identification of single atom columns in the microstructure. A good example applied in LIBs is shown in Fig. 13(b), where the layered to rock-salt phase transition is visualized by the enhanced ABF (eABF) images.[123] The increased distances between Ni–Ni* atoms are presented with a layered structure (right) transitioned to a rock-salt structure (left). The distances of O–O* atoms measured in eABF images agree well with the Ni–Ni* distances. Due to the high sensitivity to the light elements, the 4D STEM techniques are often applied to visualize the O vacancies or the cathode/electrolyte interface in LIBs.[124,125] However, very limited studies based on the 4D STEM on SIB layered oxides are reported, mainly due to the challenges of long acquisition time, high ion doses, and reconstruction algorithms. Fig. 13(c) shows a good example of the 4D STEM technique applied in the $Na_3Ni_2SbO_6$ cathode to track the ion migration under low ion doses.[126] One could see the Na vacancies formed on the surface gradually migrated into the bulk area. This work highlights the migration of Na vacancies rather than TM ions, providing a clear view of Na extraction from the bulk. It also demonstrates the influence of ion doses during 4D STEM acquisition.

It is worth noting that few studies are reported on layered oxides based on in situ TEM. Very limited in situ TEM studies have been reported based on the dynamic sodiation process and thermal stability of SIBs.[127–129] Plenty of reports focus on the charge storage mechanism in the anode materials.[130–132] The major problem lies in the selection of appropriate electrolytes which should be both applicable to the high-vacuum TEM column and stable under the high-energy electron beam irradiation.[133] At present, high-resolution STEM observations are hardly applied to most electrolytes at the atomic scale, even for the LIB study.

In summary, the integration of diverse TEM-based techniques is emerging as a key approach to overcoming challenges in structural characterization. Equipped with various spectroscopy and imaging techniques, researchers can gain a comprehensive and atomic-level insight into layered oxides for SIB systems. This approach aids in understanding the entire crystal structure, including elemental information such as TM valence evolution and concentration distributions in battery materials. Future endeavours in employing TEM techniques for battery studies should emphasize exploring innovative in situ configurations for the cathode/electrolyte interface study and enhancing both energy and spatial resolutions. Ultimately, this promising research direction offers new insights and broadens the potential for future advancements.

Data availability

No primary research results, software or code have been included in this review.

Conflicts of interest

There are no conflicts to declare.

Acknowledgements

References

1 C. Delmas, Adv. Energy Mater., 2018, 8, 1703137.
2 P. K. Nayak, L. Yang, W. Brehm and P. Adelhelm, Angew. Chem., Int. Ed., 2018, 57, 102–120.
3 Y. Gupta, P. Siwatch, R. Karwasra, K. Sharma and S. Tripathi, Renewable Sustainable Energy Rev., 2024, 192, 114167.
4 Y. Li, G. Liu, J. Che, L. Chen, X. Wang, G. Wang, L. Lei, J. Hou, S. Li, J. Wang, Y. Xu and Y. Zhao, Interdiscip. Mater., 2024, 4, 24–51.
5 Y. Chu, J. Zhang, Y. Zhang, Q. Li, Y. Jia, X. Dong, J. Xiao, Y. Tao and Q.-H. Yang, Adv. Mater., 2023, 35, 2212186.
6 S. Qiao, Q. Zhou, M. Ma, H. K. Liu, S. X. Dou and S. Chong, ACS Nano, 2023, 17, 11220–11252.
7 H. Zhang, Y. Gao, X. Liu, L. Zhou, J. Li, Y. Xiao, J. Peng, J. Wang and S.-L. Chou, Adv. Energy Mater., 2023, 13, 2300149.
8 W. Zuo, A. Innocenti, M. Zarrabeitia, D. Bresser, Y. Yang and S. Passerini, Acc. Chem. Res., 2023, 56, 284–296.
9 Q. Shen, Y. Liu, L. Jiao, X. Qu and J. Chen, Energy Storage Mater., 2021, 35, 400–430.
10 R.-M. Gao, Z.-J. Zheng, P.-F. Wang, C.-Y. Wang, H. Ye and F.-F. Cao, Energy Storage Mater., 2020, 30, 9–26.

11 R. F. Ziesche, T. M. Heenan, P. Kumari, J. Williams, W. Li, M. E. Curd, T. L. Burnett, I. Robinson, D. J. Brett and M. J. Ehrhardt, *Adv. Energy Mater.*, 2023, 2300103.

12 Y. Yuan, K. Amine, J. Lu and R. Shahbazian-Yassar, *Nat. Commun.*, 2017, **8**, 15806.

13 F. Haguenau, P. Hawkes, J. Hutchison, B. Satiat-Jeunemaître, G. Simon and D. Williams, *Microsc. Microanal.*, 2003, **9**, 96–138.

14 D. B. Williams and C. B. Carter, *Transmission Electron Microscopy: A Textbook for Materials Science*, Springer, 1996.

15 P. D. L. Nellist and S. J. Pennycook, *Adv. Imaging Electron Phys.*, 2000, **113**, 147.

16 E. Liberti, J. G. Lozano, M. P. Osorio, M. R. Roberts, P. G. Bruce and A. I. Kirkland, *Ultramicroscopy*, 2020, **210**, 112914.

17 Y. Wen, T. Shang and L. Gu, *Microscopy*, 2017, **66**, 25–38.

18 B. D. Levin and D. A. Muller, *Microsc. Microanal.*, 2015, **21**, 1549–1550.

19 K. Kubota, N. Yabuuchi, H. Yoshida, M. Dahbi and S. Komaba, *MRS Bull.*, 2014, **39**, 416–422.

20 C. Delmas, C. Fouassier and P. Hagenmuller, *Physica B+C*, 1980, **99**, 81–85.

21 L. Yang, J. M. L. del Amo, Z. Shadike, S.-M. Bak, F. Bonilla, M. Galceran, P. K. Nayak, J. R. Buchheim, X.-Q. Yang, T. Rojo and P. Adelhelm, *Adv. Funct. Mater.*, 2020, **30**, 2003364.

22 X. G. Yuan, Y. J. Guo, L. Gan, X. A. Yang, W. H. He, X. S. Zhang, Y. X. Yin, S. Xin, H. R. Yao and Z. Huang, *Adv. Funct. Mater.*, 2022, **32**, 2111466.

23 P. Yang, C. Zhang, M. Li, X. Yang, C. Wang, X. Bie, Y. Wei, G. Chen and F. Du, *ChemPhysChem*, 2015, **16**, 3408–3412.

24 N. Jiang, Q. Liu, J. Wang, W. Yang, W. Ma, L. Zhang, Z. Peng and Z. Zhang, *Small*, 2021, **17**, 2007103.

25 C. Zhao, Z. Yao, Q. Wang, H. Li, J. Wang, M. Liu, S. Ganapathy, Y. Lu, J. Cabana and B. Li, *J. Am. Chem. Soc.*, 2020, **142**, 5742–5750.

26 T. Song, C. Wang, L. Kang, W. Yao, H. Wang, H. Chen, Q. Liu, Y. Lu, Z. Guan, A. Zhu, T. Kang, Y. Tang and C.-S. LEE, *Adv. Energy Mater.*, 2023, **13**, 2302393.

27 B. Sambandam, M. H. Alfaruqi, S. Park, S. Lee, S. Kim, J. Lee, V. Mathew, J.-Y. Hwang and J. Kim, *ACS Appl. Mater. Interfaces*, 2021, **13**, 53877–53891.

28 Z. Cheng, B. Zhao, Y.-J. Guo, L. Yu, B. Yuan, W. Hua, Y.-X. Yin, S. Xu, B. Xiao, X. Han, P.-F. Wang and Y.-G. Guo, *Adv. Energy Mater.*, 2022, **12**, 2103461.

29 P.-F. Wang, Y. You, Y.-X. Yin, Y.-S. Wang, L.-J. Wan, L. Gu and Y.-G. Guo, *Angew. Chem., Int. Ed.*, 2016, **55**, 7445–7449.

30 P.-F. Wang, M. Weng, Y. Xiao, Z. Hu, Q. Li, M. Li, Y.-D. Wang, X. Chen, X. Yang, Y. Wen, Y.-X. Yin, S. Yu, Y. Xiao, J. Zheng, L.-J. Wan, F. Pan and Y.-G. Guo, *Adv. Mater.*, 2019, **31**, 1903483.

31 Q. Li, S. Xu, S. Guo, K. Jiang, X. Li, M. Jia, P. Wang and H. Zhou, *Adv. Mater.*, 2020, **32**, 1907936.

32 Y. Jin, Y. Zhao, J. Feng, S. Chen, Q. Fan, Q. Kuang and Y. Dong, *ACS Appl. Mater. Interfaces*, 2022, **14**, 56715–56724.

33 Z. Hu, M. Weng, Z. Chen, W. Tan, S. Li and F. Pan, *Nano Energy*, 2021, **83**, 105834.

34 L. Yu, X.-X. Xing, S.-Y. Zhang, X. Zhang, X. Han, P.-F. Wang and S. Xu, *ACS Appl. Mater. Interfaces*, 2021, **13**, 32948–32956.

35 L. Xiao, Z. Ding, Q. Huang, C. Chen, Y. Feng, C. Liang, P. Gao and W. Wei, *Acta Mater.*, 2020, **199**, 34–41.

36 R. A. House, U. Maitra, M. A. Pérez-Osorio, J. G. Lozano, L. Jin, J. W. Somerville, L. C. Duda, A. Nag, A. Walters, K.-J. Zhou, M. R. Roberts and P. G. Bruce, *Nature*, 2020, **577**, 502–508.

37 Q. Wang, Y. Liao, X. Jin, C. Cheng, S. Chu, C. Sheng, L. Zhang, B. Hu, S. Guo and H. Zhou, *Angew. Chem., Int. Ed.*, 2022, **61**, e202206625.

38 Z. Wu, Y. Ni, S. Tan, E. Hu, L. He, J. Liu, M. Hou, P. Jiao, K. Zhang and F. Cheng, *J. Am. Chem. Soc.*, 2023, **145**, 9596–9606.

39 W. Li, Q. Lai, X.-W. Gao, D. Yang, L. Wen, Z. Liu and W.-B. Luo, *Small*, 2024, 2406453.

40 Z. Cheng, X.-Y. Fan, L. Yu, W. Hua, Y.-J. Guo, Y.-H. Feng, F.-D. Ji, M. Liu, Y.-X. Yin, X. Han, Y.-G. Guo and P.-F. Wang, *Angew. Chem., Int. Ed.*, 2022, **61**, e202117728.

41 N. Jiang, Q. Liu, J. Wang, W. Yang, W. Ma, L. Zhang, Z. Peng and Z. Zhang, *Small*, 2021, **17**, 2007103.

42 Y.-N. Zhou, P.-F. Wang, Y.-B. Niu, Q. Li, X. Yu, Y.-X. Yin, S. Xu and Y.-G. Guo, *Nano Energy*, 2019, **55**, 143–150.

43 C. Chen, W. Huang, Y. Li, M. Zhang, K. Nie, J. Wang, W. Zhao, R. Qi, C. Zuo, Z. Li, H. Yi and F. Pan, *Nano Energy*, 2021, **90**, 106504.

44 M. Keller, D. Buchholz and S. Passerini, *Adv. Energy Mater.*, 2016, **6**, 1501555.

45 S.-Y. Zhang, Y.-J. Guo, Y.-N. Zhou, X.-D. Zhang, Y.-B. Niu, E.-H. Wang, L.-B. Huang, P.-F. An, J. Zhang, X.-A. Yang, Y.-X. Yin, S. Xu and Y.-G. Guo, *Small*, 2021, **17**, 2007236.

46 Y. Xiao, N. M. Abbasi, Y.-F. Zhu, S. Li, S.-J. Tan, W. Ling, L. Peng, T. Yang, L. Wang, X.-D. Guo, Y.-X. Yin, H. Zhang and Y.-G. Guo, *Adv. Funct. Mater.*, 2020, **30**, 2001334.

47 E. Gabriel, C. Ma, K. Graff, A. Conrado, D. Hou and H. Xiong, *eScience*, 2023, **3**, 100139.

48 S. Guo, P. Liu, H. Yu, Y. Zhu, M. Chen, M. Ishida and H. Zhou, *Angew. Chem., Int. Ed.*, 2015, **54**, 5894–5899.

49 E. Lee, J. Lu, Y. Ren, X. Luo, X. Zhang, J. Wen, D. Miller, A. DeWahl, S. Hackney, B. Key, D. Kim, M. D. Slater and C. S. Johnson, *Adv. Energy Mater.*, 2014, **4**, 1400458.

50 C. Chen, Z. Han, S. Chen, S. Qi, X. Lan, C. Zhang, L. Chen, P. Wang and W. Wei, *ACS Appl. Mater. Interfaces*, 2020, **12**, 7144–7152.

51 C. Zhao, F. Ding, Y. Lu, L. Chen and Y.-S. Hu, *Angew. Chem., Int. Ed.*, 2020, **59**, 264–269.

52 H. Wang, X. Gao, S. Zhang, Y. Mei, L. Ni, J. Gao, H. Liu, N. Hong, B. Zhang, F. Zhu, W. Deng, G. Zou, H. Hou, X.-Y. Cao, H. Chen and X. Ji, *ACS Nano*, 2023, **17**, 12530–12543.

53 H. Gao, J. Li, F. Zhang, C. Li, J. Xiao, X. Nie, G. Zhang, Y. Xiao, D. Zhang, X. Guo, Y. Wang, Y.-M. Kang, G. Wang and H. Liu, *Adv. Energy Mater.*, 2024, **14**, 2304529.

54 Q. He, J. Li, W. Liu, J. Zhang, K. Wang, J. Liu, J. Hui and H. Zhang, *J. Power Sources*, 2024, **619**, 235207.

55 E. P. George, D. Raabe and R. O. Ritchie, *Nat. Rev. Mater.*, 2019, **4**, 515–534.

56 X. Gao, X. Zhang, X. Liu, Y. Tian, Q. Cai, M. Jia and X. Yan, *Small Methods*, 2023, **7**, 2300152.

57 X. Zou, Y.-R. Zhang, Z.-P. Huang, K. Yue and Z.-H. Guo, *Chem. Commun.*, 2023, **59**, 13535–13550.

58 J. Mu, T. Cai, W. Dong, C. Zhou, Z. Han and F. Huang, *Chem. Eng. J.*, 2023, **471**, 144403.

59 Y. Ma, Y. Hu, Y. Pramudya, T. Diemant, Q. Wang, D. Goonetilleke, Y. Tang, B. Zhou, H. Hahn, W. Wenzel, M. Fichtner, Y. Ma, B. Breitung and T. Brezesinski, *Adv. Funct. Mater.*, 2022, **32**, 2202372.

60 A. Joshi, S. Chakrabarty, S. H. Akella, A. Saha, A. Mukherjee, B. Schmerling, M. Ejgenberg, R. Sharma and M. Noked, *Adv. Mater.*, 2023, **35**, 2304440.

61 J. Zhan, J. Huang, Z. Li, J. Yuan, S.-X. Dou, H.-K. Liu and C. Wu, *Nano Lett.*, 2024, **24**, 9793–9800.

62 B. Wang, J. Ma, K. Wang, D. Wang, G. Xu, X. Wang, Z. Hu, C.-W. Pao, J.-L. Chen, L. Du, X. Du and G. Cui, *Adv. Energy Mater.*, 2024, **14**, 2401090.

63 Z. Liu, R. Liu, S. Xu, J. Tian, J. Li, H. Li, T. Yu, S. Chu, A. M. D'Angelo, W. K. Pang, L. Zhang, S. Guo and H. Zhou, *Angew. Chem., Int. Ed.*, 2024, **63**, e202405620.

64 T. Cai, M. Cai, J. Mu, S. Zhao, H. Bi, W. Zhao, W. Dong and F. Huang, *Nano-Micro Lett.*, 2023, **16**, 10.

65 J. Xu, Z. Han, K. Jiang, P. Bai, Y. Liang, X. Zhang, P. Wang, S. Guo and H. Zhou, *Small*, 2020, **16**, 1904388.

66 K. Wang, P. Yan and M. Sui, *Nano Energy*, 2018, **54**, 148–155.

67 Z. Huang, S. Wang, X. Guo, F. Marlton, Y. Fan, W.-K. Pang, T. Huang, J. Xiao, D. Li, H. Liu, Q. Gu, C.-C. Yang, C.-L. Dong, B. Sun and G. Wang, *Adv. Mater.*, 2024, 2410857.

68 H. Yan, D. Chai, X. Li and Y. Fu, *Small*, 2024, 2404039.

69 Y. Liu, X. Fang, A. Zhang, C. Shen, Q. Liu, H. A. Enaya and C. Zhou, *Nano Energy*, 2016, **27**, 27–34.

70 J. H. Jo, J. U. Choi, A. Konarov, H. Yashiro, S. Yuan, L. Shi, Y.-K. Sun and S.-T. Myung, *Adv. Funct. Mater.*, 2018, **28**, 1705968.

71 L. Zhou, Z. Zhang, S. Lv, M. Zhang, P. Jiao, W. Zhang, J. Xu and K. Zhang, *Mater. Today Energy*, 2023, **38**, 101450.

72 X. Luo, Q. Huang, Y. Feng, C. Zhang, C. Liang, L. Zhou and W. Wei, *ACS Appl. Mater. Interfaces*, 2022, **14**, 51846–51854.

73 N. Jiang, J. Yu, Z. Wu, J. Zhao, Y. Zeng, H. Li, M. Meng, Y. He, P. Jiao, H. Pan, H. Wang, J. Qi, Z. Hu, K. Zhang and J. Chen, *Angew. Chem., Int. Ed.*, 2024, **63**, e202410080.

74 B. M. De Boisse, J.-H. Cheng, D. Carlier, M. Guignard, C.-J. Pan, S. Bordere, D. Filimonov, C. Drathen, E. Suard and B.-J. Hwang, *J. Mater. Chem. A*, 2015, **3**, 10976–10989.

75 S. Komaba, N. Yabuuchi, T. Nakayama, A. Ogata, T. Ishikawa and I. Nakai, *Inorg. Chem.*, 2012, **51**, 6211–6220.

76 E. Talaie, V. Duffort, H. L. Smith, B. Fultz and L. F. Nazar, *Energy Environ. Sci.*, 2015, **8**, 2512–2523.

77 J. Wang, Y.-F. Zhu, Y. Su, J.-X. Guo, S. Chen, H.-K. Liu, S.-X. Dou, S.-L. Chou and Y. Xiao, *Chem. Soc. Rev.*, 2024, **53**, 4230–4301.

78 Y. Xie, H. Wang, G. Xu, J. Wang, H. Sheng, Z. Chen, Y. Ren, C. J. Sun, J. Wen and J. Wang, *Adv. Energy Mater.*, 2016, **6**, 1601306.

79 T. Zhang, M. Ren, Y. Huang, F. Li, W. Hua, S. Indris and F. Li, *Angew. Chem., Int. Ed.*, 2024, **63**, e202316949.

80 L. Yao, P. Zou, C. Wang, J. Jiang, L. Ma, S. Tan, K. A. Beyer, F. Xu, E. Hu and H. L. Xin, *Adv. Energy Mater.*, 2022, **12**, 2201989.

81 X. Wang, Q. Zhang, C. Zhao, H. Li, B. Zhang, G. Zeng, Y. Tang, Z. Huang, I. Hwang, H. Zhang, S. Zhou, Y. Qiu, Y. Xiao, J. Cabana, C.-J. Sun, K. Amine, Y. Sun, Q. Wang, G.-L. Xu, L. Gu, Y. Qiao and S.-G. Sun, *Nat. Energy*, 2024, **9**, 184–196.

82 J. W. Somerville, A. Sobkowiak, N. Tapia-Ruiz, J. Billaud, J. G. Lozano, R. A. House, L. C. Gallington, T. Ericsson, L. Häggström and M. R. Roberts, *Energy Environ. Sci.*, 2019, **12**, 2223–2232.

83 N. Yabuuchi, M. Kajiyama, J. Iwatate, H. Nishikawa, S. Hitomi, R. Okuyama, R. Usui, Y. Yamada and S. Komaba, *Nat. Mater.*, 2012, **11**, 512–517.

84 S. Guo, P. Liu, Y. Sun, K. Zhu, J. Yi, M. Chen, M. Ishida and H. Zhou, *Angew. Chem., Int. Ed.*, 2015, **54**, 11701–11705.

85 L. Liu, X. Li, S.-H. Bo, Y. Wang, H. Chen, N. Twu, D. Wu and G. Ceder, *Adv. Energy Mater.*, 2015, **5**, 1500944.

86 R. J. Clément, J. Billaud, A. Robert Armstrong, G. Singh, T. Rojo, P. G. Bruce and C. P. Grey, *Energy Environ. Sci.*, 2016, **9**, 3240–3251.

87 Y. Tang, Q. Zhang, W. Zuo, S. Zhou, G. Zeng, B. Zhang, H. Zhang, Z. Huang, L. Zheng, Z. Xu, W. Yin, Y. Qiu, Y. Xiao, Q. Zhang, T. Zhao, H.-G. Liao, I. Hwang, C.-J. Sun, K. Amine, Q. Wang, Y. Sun, G.-L. Xu, L. Gu, Y. Qiao and S.-G. Sun, *Nat. Sustainability*, 2024, **7**, 348–359.

88 A. Singer, M. Zhang, S. Hy, D. Cela, C. Fang, T. A. Wynn, B. Qiu, Y. Xia, Z. Liu, A. Ulvestad, N. Hua, J. Wingert, H. Liu, M. Sprung, A. V. Zozulya, E. Maxey, R. Harder, Y. S. Meng and O. G. Shpyrko, *Nat. Energy*, 2018, **3**, 641–647.

89 P. Yan, J. Zheng, M. Gu, J. Xiao, J.-G. Zhang and C.-M. Wang, *Nat. Commun.*, 2017, **8**, 14101.

90 F. Ding, P. Ji, Z. Han, X. Hou, Y. Yang, Z. Hu, Y. Niu, Y. Liu, J. Zhang, X. Rong, Y. Lu, H. Mao, D. Su, L. Chen and Y.-S. Hu, *Nat. Energy*, 2024, **9**, 1529–1539.

91 L. Zhang, C. Wang, Y. Liu, M. Ren, J. Du, A. Chen and F. Li, *Chem. Eng. J.*, 2021, **426**, 130813.

92 K. Zhang, D. Kim, Z. Hu, M. Park, G. Noh, Y. Yang, J. Zhang, V. W.-H. Lau, S.-L. Chou and M. Cho, *Nat. Commun.*, 2019, **10**, 5203.

93 Y. Liu, C. Wang, S. Zhao, L. Zhang, K. Zhang, F. Li and J. Chen, *Chem. Sci.*, 2021, **12**, 1062–1067.

94 L. Sun, Z. Wu, M. Hou, Y. Ni, H. Sun, P. Jiao, H. Li, W. Zhang, L. Zhang, K. Zhang, F. Cheng and J. Chen, *Energy Environ. Sci.*, 2024, **17**, 210–218.

95 Y. Shi, S. Li, A. Gao, J. Zheng, Q. Zhang, X. Lu, L. Gu and D. Cao, *ACS Appl. Mater. Interfaces*, 2019, **11**, 24122–24131.

96 D. Susanto, M. K. Cho, G. Ali, J.-Y. Kim, H. J. Chang, H.-S. Kim, K.-W. Nam and K. Y. Chung, *Chem. Mater.*, 2019, **31**, 3644–3651.

97 S. Guo, Y. Sun, J. Yi, K. Zhu, P. Liu, Y. Zhu, G.-Z. Zhu, M. Chen, M. Ishida and H. Zhou, *NPG Asia Mater.*, 2016, **8**, e266.

98 R. Berthelot, D. Carlier and C. Delmas, *Nat. Mater.*, 2011, **10**, 74–80.

99 M. Guignard, C. Didier, J. Darriet, P. Bordet, E. Elkaïm and C. Delmas, *Nat. Mater.*, 2013, **12**, 74–80.

100 P. F. Wang, H. R. Yao, X. Y. Liu, Y. X. Yin, J. N. Zhang, Y. Wen, X. Yu, L. Gu and Y. G. Guo, *Sci. Adv.*, 2018, **4**, eaar6018.

101 L.-Y. Kong, H.-X. Liu, Y.-F. Zhu, J.-Y. Li, Y. Su, H.-W. Li, H.-Y. Hu, Y.-F. Liu, M.-J. Yang, Z.-C. Jian, X.-B. Jia, S.-L. Chou and Y. Xiao, *Sci. China: Chem.*, 2024, **67**, 191–213.

102 J. A. K. Satrughna, A. Kanwade, A. Srivastava, M. K. Tiwari, S. C. Yadav, S. Teja Akula and P. M. Shirage, *Mater. Today*, 2023.

103 M. Ren, S. Zhao, S. Gao, T. Zhang, M. Hou, W. Zhang, K. Feng, J. Zhong, W. Hua, S. Indris, K. Zhang, J. Chen and F. Li, *J. Am. Chem. Soc.*, 2023, **145**, 224–233.

104 Y. Li, X. Li, C. Du, H. Sun, Y. Zhang, Q. Liu, T. Yang, J. Zhao, C. Delmas, S. J. Harris, H. Chen, Q. Huang, Y. Tang, L. Zhang, T. Zhu and J. Huang, *ACS Energy Lett.*, 2021, **6**, 3960–3969.

105 J. Lee, A. Urban, X. Li, D. Su, G. Hautier and G. Ceder, *Science*, 2014, **343**, 519–522.

106 H. J. Yu, H. M. Qian, M. R. Otani, D. M. Tang, S. H. Guo, Y. B. Zhu and H. S. Zhou, *Energy Environ. Sci.*, 2014, **7**, 1068–1078.

107 E. Talaie, V. Duffort, H. L. Smith, B. Fultz and L. F. Nazar, *Energy Environ. Sci.*, 2015, **8**, 2512–2523.

108 X. Zhang, S. Guo, P. Liu, Q. Li, S. Xu, S. Liu, K. Jiang, P. He, M. Chen, P. Wang and H. Zhou, *Adv. Energy Mater.*, 2019, **9**, 1900189.

109 C. Chen, Z. Ding, Z. Han, C. Liang, X. Lan, P. Wang, P. Gao and W. Wei, *J. Phys. Chem. Lett.*, 2020, **11**, 5464–5470.

110 T. Jin, P.-F. Wang, Q.-C. Wang, K. Zhu, T. Deng, J. Zhang, W. Zhang, X.-Q. Yang, L. Jiao and C. Wang, *Angew. Chem., Int. Ed.*, 2020, **59**, 14511–14516.

111 T.-Y. Yu, H.-H. Ryu, G. Han and Y.-K. Sun, *Adv. Energy Mater.*, 2020, **10**, 2001609.

112 P. Yan, J. Zheng, T. Chen, L. Luo, Y. Jiang, K. Wang, M. Sui, J.-G. Zhang, S. Zhang and C. Wang, *Nat. Commun.*, 2018, **9**, 2437.

113 X. Yang, L. Zhang, G. Liu, G. Pang, D. Wang, M. Li, C. Li, Z. Liao, Q. Li, C. Zhao, J. Liang, P. Yan, K. Wang, B. Xiao and D. Geng, *ACS Appl. Mater. Interfaces*, 2024, **16**, 40805–40813.

114 G.-L. Xu, X. Liu, X. Zhou, C. Zhao, I. Hwang, A. Daali, Z. Yang, Y. Ren, C.-J. Sun, Z. Chen, Y. Liu and K. Amine, *Nat. Commun.*, 2022, **13**, 436.

115 K. Kubota and S. Komaba, *J. Electrochem. Soc.*, 2015, **162**, A2538.

116 Z. Fang, M. P. Confer, Y. Wang, Q. Wang, M. R. Kunz, E. J. Dufek, B. Liaw, T. M. Klein, D. A. Dixon and R. Fushimi, *J. Am. Chem. Soc.*, 2021, **143**, 10261–10274.

117 Y. You, A. Dolocan, W. Li and A. Manthiram, *Nano Lett.*, 2019, **19**, 182–188.

118 W. Zuo, J. Qiu, X. Liu, F. Ren, H. Liu, H. He, C. Luo, J. Li, G. F. Ortiz, H. Duan, J. Liu, M.-S. Wang, Y. Li, R. Fu and Y. Yang, *Nat. Commun.*, 2020, **11**, 3544.

119 Y. Yang, Z. Wang, C. Du, B. Wang, X. Li, S. Wu, X. Li, X. Zhang, X. Wang, Y. Niu, F. Ding, X. Rong, Y. Lu, N. Zhang, J. Xu, R. Xiao, Q. Zhang, X. Wang, W. Yin, J. Zhao, L. Chen, J. Huang and Y.-S. Hu, *Science*, 2024, **385**, 744–752.

120 B. Y. Song, Z. Y. Ding, C. S. Allen, H. Sawada, F. C. Zhang, X. Q. Pan, J. Warner, A. I. Kirkland and P. Wang, *Phys. Rev. Lett.*, 2018, **121**, 6.

121 Z. Chen, Y. Jiang, Y. T. Shao, M. E. Holtz, M. Odstrcil, M. Guizar-Sicairos, I. Hanke, S. Ganschow, D. G. Schlom and D. A. Muller, *Science*, 2021, **372**, 826–831.

122 Y. Jiang, Z. Chen, Y. M. Hang, P. Deb, H. Gao, S. E. Xie, P. Purohit, M. W. Tate, J. Park, S. M. Gruner, V. Elser and D. A. Muller, *Nature*, 2018, **559**, 343–349.

123 S. Ahmed, M. Bianchini, A. Pokle, M. S. Munde, P. Hartmann, T. Brezesinski, A. Beyer, J. Janek and K. Volz, *Adv. Energy Mater.*, 2020, **10**, 2001026.

124 N. Šimić, A. Jodlbauer, M. Oberaigner, M. Nachtnebel, S. Mitsche, H. M. R. Wilkening, G. Kothleitner, W. Grogger, D. Knez and I. Hanzu, *Adv. Energy Mater.*, 2024, **14**, 2304381.

125 N. C. Paranamana, A. Werbrouck, A. K. Datta, X. He and M. J. Young, *Adv. Energy Mater.*, 2024, 2403904, DOI: 10.1002/aenm.202403904.

126 K. Qu, J. Zhang, H. Wang, F. Wu, H. Lin, J. Chen, Z. Ding, Z. Yang and P. Gao, *Nano Today*, 2024, **59**, 102523.

127 S. Hwang, Y. Lee, E. Jo, K. Y. Chung, W. Choi, S. M. Kim and W. Chang, *ACS Appl. Mater. Interfaces*, 2017, **9**, 18883–18888.

128 Z. Li, M. Dadsetan, J. Gao, S. Zhang, L. Cai, A. Naseri, M. E. Jimenez-Castaneda, T. Filley, J. T. Miller, M. J. Thomson and V. G. Pol, *Adv. Energy Mater.*, 2021, **11**, 2101764.

129 D. Hou, E. Gabriel, K. Graff, T. Li, Y. Ren, Z. Wang, Y. Liu and H. Xiong, *J. Mater. Res.*, 2022, **37**, 1156–1163.

130 C. Y. Zhu, F. Xu, H. H. Min, Y. Huang, W. W. Xia, Y. T. Wang, Q. Y. Xu, P. Gao and L. T. Sun, *Adv. Funct. Mater.*, 2017, **27**, 1606163.

131 Y. B. Xu, K. Wang, Z. P. Yao, J. Kang, D. Lam, D. Yang, W. Ai, C. Wolverton, M. C. Hersam, Y. Huang, W. Huang, V. P. Dravid and J. S. Wu, *Small*, 2021, **17**, 2100637.

132 M. G. Boebinger, D. Yeh, M. Xu, C. Miles, B. L. Wang, M. Papakyriakou, J. A. Lewis, N. P. Kondekar, F. J. Q. Cortes, S. Hwang, X. H. Sang, D. Su, R. R. Unocic, S. M. Xia, T. Zhu and M. T. McDowell, *Joule*, 2018, **2**, 1783–1799.

133 C. Zhang, Y. Feng, Z. Han, S. Gao, M. Wang and P. Wang, *Adv. Mater.*, 2019, **32**, 1903747.